JACS
JOURNAL OF THE AMERICAN CHEMICAL SOCIETY
Article
pubs.acs.org/JACS

Hexagonal-Diamond-like Gold Lattices, Ba and $(Au,T)_3$ Interstitials, and Delocalized Bonding in a Family of Intermetallic Phases $Ba_2Au_6(Au,T)_3$ (T = Zn, Cd, Ga, In, or Sn)

Qisheng Lin, Trinath Mishra, and John D. Corbett*

Department of Chemistry, Iowa State University, Ames, Iowa 50011, United States

Supporting Information

ABSTRACT: Au-rich polar intermetallics exhibit a wide variety of structural motifs, and this hexagonal-diamond-like gold host is unprecedented. The series $Ba_2Au_6(Au,T)_3$ (T = Zn, Cd, Ga, In, or Sn), synthesized through fusion of the elements at 700−800 °C followed by annealing at 400−500 °C, occur in space group $R\bar{3}c$ ($a \approx 8.6$−8.9 Å, $c \approx 21.9$−22.6 Å, and $Z = 6$). Their remarkable structure, generated by just three independent atoms, features a hexagonal-diamond-like gold superstructure in which tunnels along the 3-fold axes are systematically filled by interstitial Ba atoms (blue) and triangles of disordered $(Au,T)_3$ atoms (green) in 2:1 proportions. The Au/Zn mixing in the latter spans ∼34 to 87% Zn, whereas the Au/Sn result is virtually invariant compositionally. Complementary bonding between the gold lattice and the disordered $(Au,T)_3$ units is substantial and very regular. Bonding and charge density analyses indicate delocalized bonding within the gold host and the $(Au,T)_3$ triangular units, and moderately polarized bonding between Ba and the electronegative framework. The new structure can also be viewed empirically as the result of an atom-by-triad [i.e., Ba by $(Au,T)_3$ triangle] topological substitution in a $BaAu_2$ (AlB_2-type) superstructure.

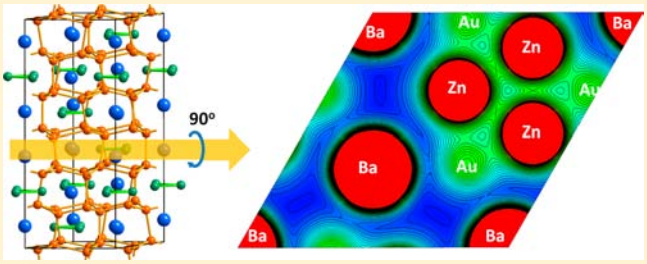

INTRODUCTION

Electron-poor polar intermetallics that have fewer than ca. 2.2 valence electrons per atom (e/a) are both poorly understood and greatly underappreciated in comparison with more electron-rich intermetallics or, particularly, molecular materials. The structural motifs and bonding patterns for these new materials are difficult to understand in terms of classical octet and Wade−Mingos rules[1,2] that are widely and effectively utilized to rationalize the more classical structures of and bonding in strongly polarized Zintl phases constructed from active metals and combinations of more electron-rich main group elements with very different electronegativities. Rather, such electron-poor polar intermetallics are more or less closer to the Hume−Rothery phases. The latter have been classically identified with α-, β-, γ-, and η-brass-type phases, which form at e/a ratios of ≈1.4, 3/2, 21/13, and 7/4, respectively, in noble metal alloys (e.g., Cu−Zn, Cu−Cd, Ag−Ga, Au−Ga, and Au−Sn),[4] regardless of the solute elements added to the noble metals.[3] Recently, some quasicrystals (QCs) and their corresponding approximants (ACs) with e/a values in the range of ca. 1.7−2.2 have also been identified as new types of Hume−Rothery phases.[4] All of these electron-poor but relatively orbitally rich systems characteristically feature high coordination numbers (12−18) for the metal atoms, as do the simple metals.

Our interest in exploratory syntheses of electron-poor Au-rich and polar intermetallics stems from many fruitful discoveries following electronic tuning of Au-based QC/ACs in the A−Au−M (A = Ca, Yb, or Na; M = Ga, In, Ge, or Sn) systems[5−10] and further explorations of related systems.[11] In these cases, we were usually able also to find other gold-rich phases that featured novel aggregates or fragments of pure Au, such as tetrahedral nets,[12,13] sinusoid layers,[14] hexagonal stars,[15] and square pyramids.[16] Such a scenario is in great contrast to more Au-poor intermetallic phases in which gold often participates in heteroatomic bonding. The plethora of new phases and structures with gold have been considered to arise in good part because of the importance of relativistic effects in the bonding of gold,[17] which lead to enhanced 6s−5d mixing in valence states as well as smaller effective radii and hence shorter bonds. Thus, Au exhibits very strong covalent bonding interactions with itself and other anionic elements; meanwhile, some d states of "cationic" elements (sodium, alkaline, or rare earth metals) fall below the E_F because of their significant covalent bonding interactions with gold and other electronegative components. Nevertheless, it is still impossible to rationalize such structures with either the Wade−Mingos concepts or a Hume−Rothery mechanism, and many diverse structural motifs remain to be explored so that insightful concepts might be derived.

Continuing our systemic studies of $AeAu_3T$ (Ae = Ca, Sr, or Ba; T = Ga, In, Ge, or Sn) compositions,[15,16,18] which were initiated to investigate isostructural analogues of the 1/0 AC

Received: February 6, 2013
Published: June 27, 2013

   dx.doi.org/10.1021/ja401378q | J. Am. Chem. Soc. 2013, 135, 11023−11031

Table 1. Some Loaded Reactions, Elemental Proportions Refined from Single-Crystal Data, Major Products and Estimated Yields, and Lattice Parameters and Volumes of the 2−6−3 Phases Refined from Powder X-ray Diffraction Data

loaded composition	refined composition	major products and estimated yields[a]	a (Å)	c (Å)	volume (Å^3)	crystal no.[b]
$Ba_2Au_6Zn_3$	$Ba_2Au_{6.40(2)}Zn_{2.60(2)}$	60% 2−6−3 + $BaAu_3Zn_2$	8.6385(5)	21.963(2)	1419.4(1)	**1**
$Ba_2Au_7Zn_2$	$Ba_2Au_{7.11(1)}Zn_{1.89(1)}$	85% 2−6−3	8.6747(5)	22.004(5)	1433.9(1)	**1s**
$Ba_2Au_8Zn_1$	$Ba_2Au_{7.89(2)}Zn_{1.11(2)}$	>95% 2−6−3	8.6762(6)	22.238(2)	1449.7(2)	**2s**
$Ba_2Au_{8.2}Zn_{0.8}$	$Ba_2Au_{7.97(2)}Zn_{1.03(2)}$	35% 2−6−3 + $BaAu_5$	8.665(1)	22.325(5)	1451.5(4)	**2**
$Ba_2Au_6Cd_3$		55% 2−6−3 + U1	8.8414(4)	22.518(2)	1524.4(1)	
$Ba_2Au_7Cd_2$	$Ba_2Au_{6.94(2)}Cd_{2.06(2)}$	>95% 2−6−3	8.8352(4)	22.510(1)	1521.7(1)	**3s**
$Ba_2Au_8Cd_1$		∼90% 2−6−3	8.7667(4)	22.591(2)	1503.6(1)	
$Ba_2Au_6Ga_3$		50% 2−6−3 + U2	8.7034(6)	21.838(3)	1432.6(2)	
$Ba_2Au_7Ga_2$	$Ba_2Au_{6.81(1)}Ga_{2.19(1)}$	>95% 2−6−3	8.7186(8)	21.816(2)	1436.2(2)	**4s**
$Ba_2Au_8Ga_1$		∼90% 2−6−3	8.7841(6)	22.232(3)	1485.6(2)	
$Ba_2Au_6In_3$		40% 2−6−3 + U3	8.8797(5)	22.544(3)	1539.4(2)	
$Ba_2Au_7In_2$	$Ba_2Au_{6.97(2)}In_{2.03(2)}$	>95% 2−6−3	8.8478(8)	22.487(3)	1524.5(3)	**5s**
$Ba_2Au_8In_1$		75% 2−6−3 + U4	8.8048(4)	22.412(1)	1504.7(1)	
$Ba_2Au_6Sn_3$		<10% 2−6−3 + U5	–	–	–	
$Ba_2Au_7Sn_2$		25% 2−6−3 + U5	8.8140(5)	22.297(2)	1500.1(2)	
$Ba_2Au_8Sn_1$	$Ba_2Au_{8.06(2)}Sn_{0.94(2)}$	70% 2−6−3 + U5	8.8112(5)	22.308(3)	1499.9(1)	**3**

[a]Yields were estimated from the strongest peaks; 2−6−3 denotes the present 2−6−3 phases and U unidentified phase(s). [b]**s** refers to single -crystal data given in Supporting Information.

$CaAu_3Ga$ ($Pa\bar{3}$),[18] led to the discovery of the unprecedented Ba_2Au_8Sn following a reaction of target composition $CaAu_3Sn$ instead of that with Ga. [The product will hereafter be written as $Ba_2Au_6(Au_2Sn)$ etc. (2−6−3) for the sake of clarity and to distinguish the two very different Au functions.] Remarkably, the "colored" structure features an unprecedented hexagonal-diamond-like gold host lattice, in which cavities in the gold channels along the c axis are regularly filled by ordered Ba atoms and $(Au,T)_3$ triangles. Later, we found that phase space for this novel structure type extends to groups 12 (T = Zn or Cd) and 13 (T = Ga or In) as well as 14 (T = Sn), but within a more or less limited e/a range for all T examples of approximately 1.3−1.6. Noteworthy variations in the Au:T proportions in the $(Au,T)_3$ triangles that run counter to the valence populations of T in turn serve to keep the e/a over the series in this lower range. In this work, the syntheses and structures of the new phases and their topological relationship with the simple binary $BaAu_2$ are presented and discussed. Theoretical analyses are also provided to help describe the moderately polarized and highly delocalized bonding states among the component atoms with their characteristically high coordination numbers.

EXPERIMENTAL SECTION

Syntheses. Dendritic Ba pieces (99.95%, Alfa Aesar), with surfaces manually cleaned by a surgical blade, as-received Au particles (99.999%, BASF), and Zn shot (99.99%), Cd shot (99.95%), Ga ingot (99.99%), In tear drop (99.99%), or Sn shot (99.99%), all from Alfa Aesar, were used as starting materials. Designed mixtures were loaded into precleaned Ta tubes ($\phi \approx 0.9$ cm) within a N_2-filled glovebox (H_2O concentration of <0.1 ppm by volume). After being transferred into an arc welder, the crimped Ta tubes were weld-sealed under argon and then enclosed in evacuated SiO_2 jackets (<10^{-5} Torr) to protect them from air during heating.

Ba_2Au_8Sn crystals were first obtained as the major product of a reaction with a nominal composition of $BaAu_3Sn$ that was run at 700 °C for 6 h, cooled to 400 °C at a rate of 2 °C/h, annealed there for 1 week, and then quenched into water. After the chemical composition had been established by a single crystal structural refinement, stoichiometric reactions to give selected $Ba_2Au_6(Au_{3-x}Sn_x)$ (x = 0, 1, 2, or 3) compositions were run under the same conditions to check the phase width. However, the powder X-ray diffraction data for the products revealed only small variations in refined lattice parameters (Table S1 of the Supporting Information), characterizing a narrow homogeneity range for the Sn phase at 400 °C and $x \sim 0.9$.

To check whether isostructural phases exist in other systems, stoichiometric $Ba_2Au_6(Au_{3-x}T_x)$ compositions (T = Zn, Cd, Ga, or In; x = 0−3) were also reacted under a revised temperature−time profile: 800 °C for 10 h, slowly cooled to 400 °C, annealed there for 2 weeks, and quenched in water. All target phases were obtained in high yields at one or more compositions; see the powder pattern data and single-crystal compositions in Table 1 and Figure S1 of the Supporting Information. However, attempts to obtain isostructural phases with T = Tl, Ge, Sb, Cu, Mn, or Mg under the same conditions were not successful. All of the 2−6−3 products have metallic lusters, and they are visually stable in air at room temperature for at least 3 months.

X-ray Powder Diffraction. Samples were first evaluated on the basis of powder diffraction data collected on a STADI P powder diffractometer equipped with Cu Kα_1 radiation (λ = 1.540598 Å). A powdered Si standard (NIST 640c) was added to each sample to calibrate peak positions, so that accurate lattice parameters could be compared directly and with diffractometer data as well. (Earlier powder data for the Sn samples were collected with the aid of a Huber G670 camera equipped with image plate and monochromated Cu Kα_1 radiation.) The detection limits of a second phase in these systems and for both instruments are conservatively estimated to be about 5 vol % in equivalent scattering power. Phase identification was conducted with the aid of PowderCell,[19] and lattice parameters were refined with the aid of UnitCell[20] from ∼10 to ∼15 reflection peaks that fell in a 2θ range of 15−70° and had no overlap with those from other phases. The loaded compositions, estimated phase distributions, semi-quantitatively refined single-crystal analyses, and refined lattice parameters for all samples studied are listed in Table 1.

Structural Determination. Single crystals from selected products were each mounted on a Bruker APEX CCD single-crystal diffractometer equipped with graphite-monochromatized Mo Kα radiation (λ = 0.71069 Å). Intensity data were collected at room temperature in an ω scan mode over 2$\theta \sim$ 7−57°. Data integration, Lorentz polarization, and other corrections were made with the SAINT subprogram included in the SMART software package.[21] Empirical absorption corrections were performed with the aid of the SADABS subprogram. Analyses of systematic reflection absences revealed that all of the new phases have the centered space group $R\bar{3}c$, whereas their lattice parameters fall within the following ranges: $a \approx$ 8.6−8.9 Å, and $c \approx$ 21.9−22.6 Å. Structure solution and refinements were performed using SHELXTL (version 6.1).

dx.doi.org/10.1021/ja401378q | J. Am. Chem. Soc. 2013, 135, 11023−11031

Table 2. Crystal Data and Structure Refinements for $Ba_2Au_6(Au,T)_3$ (T = Zn or Sn)

	1	2	3
formula	$Ba_2Au_{6.40(2)}Zn_{2.60(2)}$	$Ba_2Au_{7.97(2)}Zn_{1.03(2)}$	$Ba_2Au_{8.06(2)}Sn_{0.94(2)}$
formula weight	1705.45	1911.83	1973.54
space group/Z	$R\bar{3}c/6$	$R\bar{3}c/6$	$R\bar{3}c/6$
unit cell			
a (Å)	8.6385(5)	8.665(1)	8.8112(5)
c (Å)	21.963(2)	22.325(5)	22.308(3)
volume (Å^3)/d_{calc} (g/cm^3)	1419.4(1)/11.971	1451.5(4)/13.123	1499.9(2)/13.109
absorption coefficient	113.365	130.727	127.662
no. of reflections collcted/R_{int}	3448/0.0867	3404/0.0841	4026/0.0586
data/res./para.	395/0/20	433/0/20	417/0/20
GOF	1.015	1.038	1.039
R1/wR2 [$I > 2\sigma(I)$]	0.0311/0.0726	0.0351/0.0716	0.0227/0.0471
all data	0.0359/0.0746	0.0517/0.0771	0.0299/0.0492
extinction coefficient	0.00010(2)	0.00020(2)	0.00011(1)
residue (e/Å^3)	1.794/−2.175	3.804/−3.552	1.670/−1.581

Table 3. Atomic Coordinates (×10^4) and Equivalent Isotropic Displacement Parameters for $Ba_2Au_6(Au,T)_3$ (T = Zn or Sn)

atom[a]	Wyckoff	symmetry	x	y	z	U_{eq}[b] (×10^3 Å^2)	Au/T occupancy (%)
			(1) $Ba_2Au_{6.40(2)}Zn_{2.60(2)}$				
Au	36*f*	1	3468(1)	394(1)	155(1)	26(1)	
M	18*e*	0.2	1837(2)	0	1/4	25(1)	13.4/86.6(5)
Ba	12*c*	3	0	0	930(1)	24(1)	
			(2) $Ba_2Au_{7.97(2)}Zn_{1.03(2)}$				
Au	36*f*	1	3399(1)	385(1)	153(1)	13(1)	
M	18*e*	0.2	1864(1)	0	1/4	9(1)	65.6/34.4(7)
Ba	12*c*	3	0	0	952(1)	10(1)	
			(3) $Ba_2Au_{8.06(2)}Sn_{0.94(2)}$				
Au	36*f*	1	3331(1)	369(1)	153(1)	22(1)	
M	18*e*	0.2	1882(1)	0	1/4	18(1)	68.6/31.4(8)
Ba	12*c*	3	0	0	970(1)	20(1)	

[a]M = Au/T (T = Zn or Sn). [b]U_{eq} is defined as one-third of the trace of the orthogonalized U_{ij} tensor.

Structure determinations for all structures were quite straightforward, as exemplified by the initial solution for $Ba_2Au_{8.06(1)}Sn_{0.94(2)}$. Three independent sites were first identified by direct methods. Two sites had suitable separations for Au−Au, Au−Sn, or Sn−Sn pairs (2.7−3.1 Å) and the other for Ba−Au or Ba−Sn pairs (3.3−3.8 Å), so they were assigned to Au and Ba, respectively. Subsequent refinements revealed that Au at the 18*e* site had isotropic parameters (0.022 Å^2) slightly larger than those for the other two atoms (both ∼0.018 Å^2), indicating the former site could be occupied by an Au/Sn admixture. It was so assigned and the isotropic parameter refined as 0.017 Å^2 for a ∼70:30 proportion; meanwhile, R1 decreased from 6.11 to 4.87%. Separate refinements of the occupancy parameters of Ba and Au at the general 12*c* and 36*f* sites were also made, but full occupancies were suggested at both sites because of their small deviations (<2σ) from 100% occupancy. Final least-squares refinements, with anisotropic displacement parameters and a secondary extinction correction, yielded an R1 of 2.27%, a wR2 of 4.92%, and a GOF of 1.039 for 20 parameters refined from 417 independent observed data. The largest residual electron densities and holes in the final refinement were less than ±1.7 e$^-$/Å^3, quite good among results for phases containing major amounts of Au because of sometimes inadequate absorption corrections. Isostructural compounds obtained with T = Zn, Cd, Ga, and In were refined likewise. The Wyckoff 18*e* sites were always occupied by Au/T admixtures, and the 36*f* sites were fully occupied by Au.

To establish the true phase width for the broad Zn compound, single crystals from the four $Ba_2Au_6(Au_{3-x}Zn_x)$ reaction mixtures loaded as x = 0.8, 1, 2, and 3 were structurally refined. On the other hand, only one composition was refined from each of the Cd, Ga, In, and Sn systems (see Tables 1−3 and Tables S1 and S2 of the Supporting Information). The refinement and crystallographic parameters for the two extreme Zn compositions (crystals **1** and **2**) and that for Sn (**3**) are listed in Tables 2 and 3, whereas the parallel data for the other five refined structures [crystals **1s**−**5s** (Table 1)] are given in the Supporting Information.

LMTO−ASA Calculations. These were performed for an ordered model of the Zn phase by means of the self-consistent, tight-binding, linear-muffin-tin-orbital (LMTO) method in the local density (LDA) and atomic sphere (ASA) approximations, within the framework of the DFT method.[22−24] ASA radii were automatically scaled within the limit of 18% maximal overlap between two occupied atomic spheres, and no interstitial sphere was needed. The average ASA diameters for Ba, Au, and Zn were 4.25, 2.97, and 2.80 Å, respectively. Reciprocal space integrations were conducted by means of the tetrahedron method. The basis sets were 5d/6s/(6p) for Ba, 5d/(5f)/6s/6p for Au, and 4s/4p for Zn with orbitals in parentheses down-folded. Scalar relativistic effects were necessarily included in the calculations. The band structures were sampled for 12 × 12 × 4 k points in the irreducible wedge of the Brillouin zones. Crystal orbital Hamilton population (COHP) analyses[25] of the structure were also performed to gain insights into the bonding properties, as well as charge density calculations to elaborate delocalization effects.

RESULTS AND DISCUSSION

Phase Widths and Phase Stability. Table 1 summarizes the results of all of reactions run to produce 2−6−3 phases, the refined compositions from eight single-crystal examples, and the powder diffraction results regarding the estimated yields of the major phases and cell dimensional data for all of the 2−6−3

dx.doi.org/10.1021/ja401378q | J. Am. Chem. Soc. 2013, 135, 11023−11031

phases. The observed powder patterns for the four Zn products appear in Figure 1 to illustrate the evolution of these with

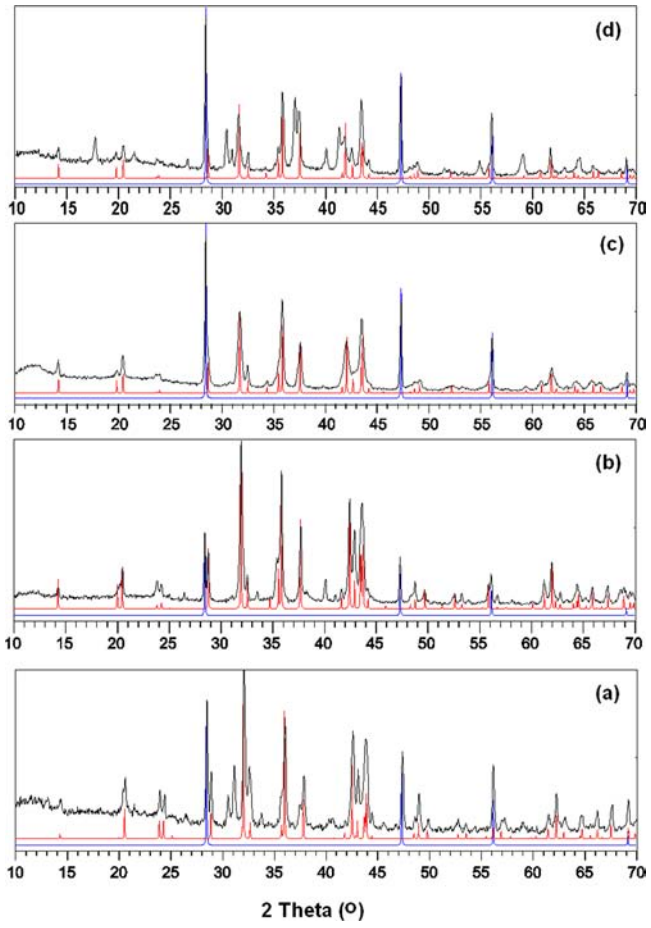

Figure 1. Powder X-ray diffraction patterns for products of $Ba_2Au_6(Au_{3-x}Zn_x)$ reactions loaded as (a) $x = 3$, (b) $x = 2$, (c) $x = 1$ (a single 2−6−3 product), and (d) $x = 0.8$ (Table 1). Black curves represent experimental data, whereas red and blue curves are calculated from single-crystal data for that 2−6−3 phase and the Si standard, respectively. Note that the products for those other than reaction c are multiphasic (see Table 1).

changes in composition as well as fits of one or more observed 2−6−3 patterns with those simulated from the corresponding single-crystal data. Like evidence regarding T = Cd, Ga, In, and Sn is in Figure S1 of the Supporting Information. At least one $Ba_2Au_6(Au_{3-x}T_x)$ product for each T = Zn, Cd, Ga, or In (but not Sn) consisted of a single 2−6−3 product by this judgment (within the probable limits of careful weighing of reactants and good X-ray powder diffraction analyses).

A close agreement achieved between measured powder patterns of "single-phase" 2−6−3 products and those calculated from the respective crystal structures was easy to achieve given sufficient routine attention to calibrations, gaining homogeneous products, and so forth. In turn, this virtual identity condition gives powerful evidence that the assigned compositions of each compound are correct, and that no further analyses are warranted. This circumstance is not common because, in general, a new compound is stoichiometrically much closer to a "line compound" (i.e., a single line on the phase diagram), so that any single crystal selected is apt to be very different from those in the mixed products of a typical randomly loaded composition. In this case, a second synthesis reaction at the refined composition of the single-crystal analysis is necessary to gain the expected close agreement between observed product and simulated powder pattern and, from this, proof that all is well. For example, secondary efforts were necessary in the recent discoveries of the novel $Ca_4Au_{10}In_3$[14] and Y_3MnAu_5.[26]

The single-crystal refinements (Experimental Section) also established that the Wyckoff 18*e* sites that define the triangular units are always occupied by Au/T mixtures and never by pure Au or pure T, whereas the 36*f* site that defines the entire host lattice is fully occupied by Au atoms. Therefore, the phase width of each 2−6−3 phase is related to only the range of Au and T proportions at the 18*e* site. Variations in lattice parameters for each T that were refined from powder data (Table 1) indicate that the ternary 2−6−3 phases formed by Zn, Cd, Ga, or In each exhibit appreciably diverse compositions that in general increase in width from Sn to Zn. Intrinsic compositional ranges were refined from single crystals from multiple loadings only for the Zn system as an example. As shown by powder pattern data in Figure 1d, the reaction of nominal $Ba_2Au_{8.2}Zn_{0.8}$ yields a mixed product of $Ba_2Au_{8.06(2)}Zn_{0.94(2)}$ and $BaAu_5$, etc., whereas the $Ba_2Au_6Zn_3$ reaction at the other extreme (a) yields an ∼3:2 mixture of $Ba_2Au_{6.40(2)}Zn_{2.60(2)}$ and $BaAu_3Zn_2$. In contrast, reactions of $Ba_2Au_7Zn_2$ (b) and Ba_2Au_8Zn (c) both yielded different compositions of the single 2−6−3 phase. Therefore, the opposed compositions refined for crystals **1** and **2**, which are each in equilibrium with the next phase as well, represent the homogeneity width of this Zn system, that is, $1.03(2) \geq x \geq 2.60(2)$ at 400 °C. Their lattice parameters *a* and *c* show substantially linear relationships with the refined composition *x* in $Ba_2Au_6(Au_{3-x}Zn_x)$ (Figure S2 of the Supporting Information) following Vegard's rule for ideal solid solutions.

The number of valence electrons per atom (e/a) for the Zn phase ranges from 1.27 to 1.42 if the Au $5d^{10}$ states are counted as a core; e/a values for other structurally characterized 2−6−3 Cd and Sn examples also fall in this range. On the other hand, the Ga and In phases have larger e/a values, 1.58 and 1.55, respectively, meaning that they act as better reducing agents for Au in the respective compounds. The cell volumes also exhibit some distinctive differences, increasing upon addition of the larger Cd or In but decreasing for added Zn or Ga (Table 1). In other words, these gross differences reflect the change in sign of the partial molar volumes of T relative to Au, positive for Cd and In but negative for Zn and Ga. The ranges of T volume increments are greater for the heavier diel (Cd) or triel (In), too, which may also reflect their stronger reducing power. Finally, the occurrence of 2−6−3 phases with elements from groups 12 (Zn and Cd), 13 (Ga and In), and 14 (Sn) but not those from group 11 (Cu) or group 15 (Sb) suggests that electronic factors over the wider range have more influence on the structural stability than the size of T, but this may reflect differences in thermodynamically competitive products, too. The latter were not systematically investigated, and some are unknown.

Structural Description. According to single-crystal X-ray diffraction analyses, our isostructural 2−6−3 compounds can be described well in the trigonal space group $R\bar{3}c$ ($a \approx 8.6$−8.9 Å, $c \approx 21.9$−22.6 Å, and $Z = 6$) (Table 2 and Table S1 of the Supporting Information), with only three independent atom sites. As illustrated in Figure 2 for T = Sn, the structures feature three components: an unprecedented hexagonal-diamond-like

dx.doi.org/10.1021/ja401378q | J. Am. Chem. Soc. 2013, 135, 11023−11031

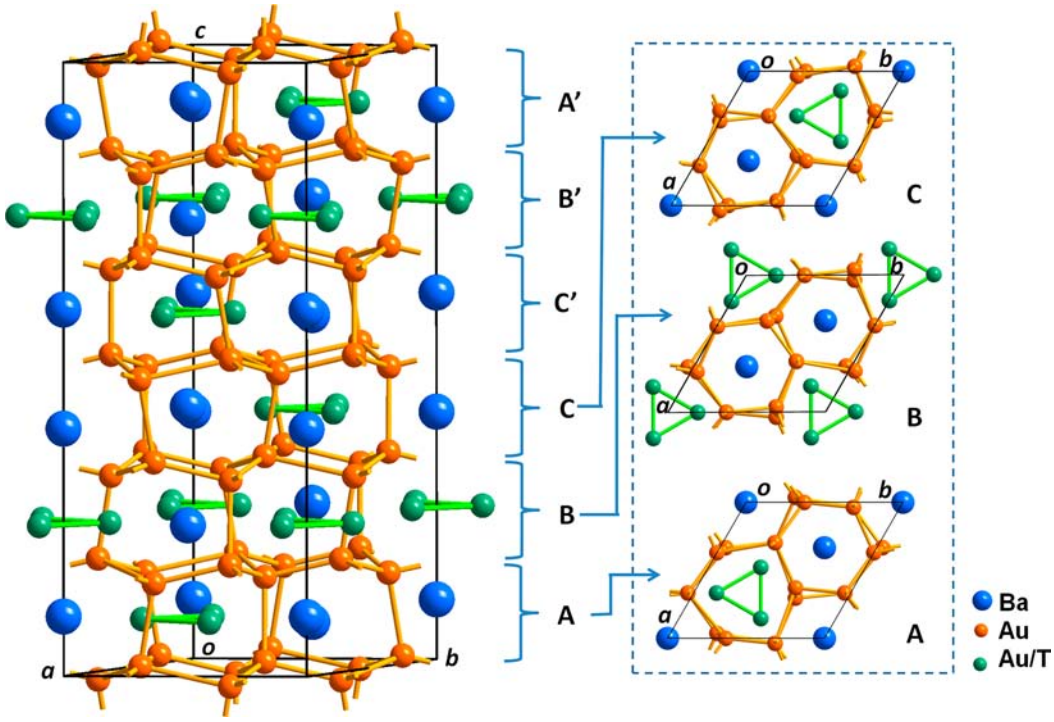

Figure 2. Structure of $Ba_2Au_6(Au,T)_3$ that consists of a hexagonal-diamond-like gold lattice stuffed with interstitial Ba (blue) and triangular $(Au,T)_3$ units (green). A, B, C, C′, B′, and A′ mark the layering sequences along the *c* axis. The inset shows projections along the *c* axis of the ordering of Ba and $(Au/T)_3$ units and the Au network in the unit cells of separate A-, B-, and C-type layers.

gold host lattice/network that bonds interstitial Ba atoms (blue) and M_3 triangles (green) generated from disordered Au/T atoms, all of which are ordered about 3-fold axes/tunnels at 0 0 *z*, $^1/_3$ $^2/_3$ $^2/_3$ + *z*, etc. It is impressive to note how effective these relatively few structural patterns, their coupled distortions, and regularities are in generating a large and very well packed structure in the large $R\bar{3}c$ cell. The Pearson symbol for this structure is *hR*66. Although there are other isopointal phases with Pearson symbol *hR*66 that utilize the same set of Wyckoff positions,[27] these exhibit different coordinates and bonding patterns, which render them as different structural types. There is no precedent whatsoever for any part of this particular structure, composition range, or bonding details; the results once again represent more of the new and unanticipated ways in which these particular elements can express a new chemistry associated with an unexplored region of phase space. Even the more-or-less comparable Sr and Ca systems give distinctly different structures, effective packing (and bonding) seeming to be major determinants in phase stabilities in such systems.[10,16]

All of the apparent complexities in the detailed structure arise first from the hexagonal-diamond-like host lattice. This entire array is generated by Au on 36*f* (*x y z*) general positions. As shown in Figure 2, prominent features of the structure are (1) puckered gold nets normal to *c*, (2) two distinctly different interstitial inserts, Ba and $(Au,T)_3$, that are tightly bound within two types of cavities that lie along the C_3 axes and between the gold layers, and (3) as a consequence of their sequence, gold tunnel walls that "wobble" along the 3-fold axes (Figure S3 of the Supporting Information) as reflected by the small non-zero value of the Au *y* coordinate (~0.015). These features are in distinct contrast to the regular hexagonal close-packed (h.c.p.) packing in the smaller $P6_3/mmc$ "hexagonal diamond" cell[28] (the natural mineral has also been called wurtzite diamond or longsdaleite[29]), which exhibits regular bond distances in h.c.p. layers and normal hexagonal tunnels along the *c* axis. These packing and distortions are also the reason that the unit cell contains six puckered, shared gold layers in the 2−6−3 structures (Figure 2). However, all puckered gold layers are symmetry-equivalent, each an ordered net of two differently sized six-membered rings that share edges (Figure S4 of the Supporting Information).

The details of the encapsulation of the Ba and M_3 between the intersections of two gold layers and the 3-fold tunnel axes express their tight binding. With the atomic environment of the electropositive Ba atom in ~$Ba_2Au_6(Au,T)_3$ as a starting point (Figure 3a), each Ba is surrounded by a single cage of 12 Au atoms with C_3 symmetry along the *c* axis, these defining two differently sized six-membered Au rings. Each ring is puckered in a *trans* configuration as viewed along the *a* or *b* direction. The smaller ring at the top contains two sets of three short and nominally equal Au−Au distances [2.877(1) Å with Sn] and equal internal angles, 114.55(2)°. [This regularity occurs because an equivalent Ba atom also lies next above it on the C_3 axis (Figure 2).] In contrast, the gold ring at the bottom of Figure 3a, identical to that at the top of Figure 3b, contains, alternately, the three longest [3.393(1) Å] and three shortest Au−Au distances [2.877(1) Å] in a ring that is shared with the $(Au/Sn)_3$ substituent below it. Correspondingly, the internal bond angles herein are also divided into two groups, 129.18(2)° and 100.91(2)° (Figure S4 of the Supporting Information). Both sets of six-membered rings are further interconnected along ±*c* by means of intermediate ~3.09 Å Au−Au bonds ("pillars") between the closest interlayer atoms (Figure 2).

Similarly, each $(Au/T)_3$ equilateral triangle is also surrounded by 12 gold atoms (Figure 3b), all at 2.723 Å (T = Sn) that define a cluster with an overall D_3 symmetry with a principal C_3 axis along the *c* axis and three perpendicular C_2

dx.doi.org/10.1021/ja401378q | J. Am. Chem. Soc. 2013, 135, 11023−11031

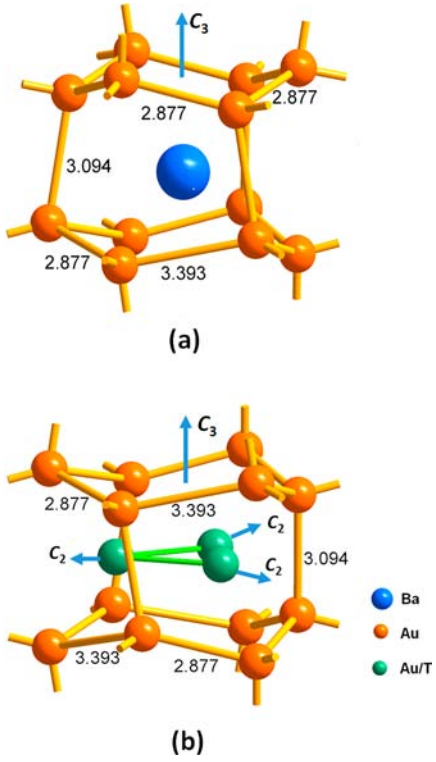

Figure 3. Environments of interstitial (a) Ba and (b) triangular $(Au,T)_3$ units between six-membered rings in the gold network in $Ba_2Au_6(Au,T)_3$. Both lie on 3-fold axes along the *c* axis, and the latter has D_3 symmetry. The distances marked are those in $Ba_2Au_{8.06}Sn_{0.94}$.

axes parallel to the *a*−*b* plane. Correspondingly, both top and bottom puckered rings are symmetrically equivalent, meaning they are the same size and are both shared with neighboring Ba atoms in the packing sequences along the *c* axis (see Figures 2 and 3a). With this information, it is easy to understand the ordering of interstitial Ba and $(Au/T)_3$ triangles in the structure with their complementary bonding within the gold net (below). Each triangular M_3 unit and its neighboring Au atoms exhibit particularly strong bonding interactions, as indicated by the short external Au−M distances (Table 4 and Table S3 of the Supporting Information) as well as other bonding parameters (below). In fact, these Au−M contrasts are even smaller than in the M−M distances within the triangular units, except in the Ga

Table 4. Important Interatomic Distances for Refined $Ba_2Au_{7.11}Zn_{1.89}$[a] and Corresponding −ICOHP Data (electronvolt per bond) for Its Idealized Ordered $Ba_2Au_7Zn_2$ Model[b]

bond	distance (Å)	−ICOHP	bond	distance (Å)	−ICOHP
Ba−Au	3.3065(8)	0.40	Au−Au	2.9156(6)	1.24
Ba−Au	3.3155(7)	0.45	Au−Au	3.016(1)	0.83
Ba−Au	3.4170(8)	0.37	Au−Au	3.142(1)	0.60
Ba−Au	3.7084(9)	0.31	Au−M	2.6676(6)	1.53
Ba−M	3.725(1)	0.22	Au−M	2.692(1)	1.68
Ba−M	3.783(1)	0.17	Au−M	2.8656(6)	1.00
Au−Au	2.9155(6)	1.23	M−M	2.729(2)	1.21

[a]Crystal data in the Supporting Information. [b]Au_3 and Zn_3 triangles are completely ordered in the model, so the ICOHP data within and related to these triangles are averaged.

phase (Table S3 of the Supporting Information). Further evidence regarding these features will be found in a subsequent theoretical study.

The distribution of Ba and $(Au,T)_3$ units in an ordered 2:1 proportion throughout the galleries in the rhombohedral unit cell naturally reflects uniform interactions over the whole cell and its $R\bar{3}c$ symmetry. As marked in Figure 2, the unit cell can be catalogued as a regular stacking of six slabs of double gold layers that sandwich Ba and M_3 according to the relative positional sequences A, B, and C plus the inverted sequences C′, B′, and A′. The projections along the *c* axis of the unit cell contents of the first three of these are shown on the right side of Figure 2, giving more details about some features already discussed, shared gold rings, distortions, and symmetry constraints in particular. The contents of the entire unit cell are generated from these three interstitial ordering arrangements and the symmetry operations of $R\bar{3}c$. A wider inspection shows that every M_3 triangle is surrounded by six next-nearest-neighbor Ba atoms in the same *a*−*b* plane and the two along the *c* axis.

Electronic Structure Approximations. The new 2−6−3 structure contains disordered Au/T mixtures around the Wyckoff 18*e* sites, but defect-free structural models are needed to conduct electronic structure calculations. Two orbital models, $Ba_2Au_7Zn_2$ ($P\bar{3}c1$) and $Ba_2Au_{7.5}Zn_{1.5}$ ($R32$), were built with the following considerations: (1) both compositions are within the homogeneity composition range of the Zn system ($2.60 \geq x \geq 1.03$), and (2) both space groups are maximal subgroups of the $R\bar{3}c$ parent group. Thus, different triangles are completely occupied by Au or Zn in both models, but the Au_3 and Zn_3 triangles occur in a 1:2 ratio in $Ba_2Au_7Zn_2$ and a 1:1 ratio in $Ba_2Au_{7.5}Zn_{1.5}$. However, both models lead to similar conclusions, so only the results of the former model are presented.

Figure 4a shows the densities of states (DOS) for the $Ba_2Au_7Zn_2$ model calculated by the DFT method. In general, the Fermi energy (E_F) falls on a continuous DOS curve, suggesting a metallic character. This character would not change between $Ba_2Au_6(Au_{0.4}Zn_{2.6})$ (e/a = 1.28) and $Ba_2Au_6(Au_2Zn)$ (e/a = 1.58) with a rigid band, as so marked for E_F. Notably, ∼19.1% of all Ba states, marked by the dashed line in panel a, fall below the E_F, reflecting its covalent bonding with Au and Zn states, mostly via Ba 5d and Au 5d to begin with. Covalent bonding between such electropositive and electronegative components is not abnormal in polar intermetallics. For example, Ba−Au covalent bonding can be clearly mapped by the electron localizability indicator (ELI) in the clathrate I-type structure of $Ba_8Au_6Ge_{46}$.[30] In the Ca-based crystalline approximants,[5−8] the mixing of Ca 3d states with s and p orbitals on the electronegative components (Ga, In, Ge, Sn, etc.) also contributes to covalent bonding between them. The projected DOS in Figure 4a also clearly show different structural functionalities for Au on 18*e* and 36*f* sites. The 36*f* states of Au (mainly 5d) are largely populated between −5.8 and −2.5 eV, similar to the behavior in other Au-rich polar intermetallics.[15,16] As a consequence, the Au_{36f}−Au_{36f} bonding within the gold network exhibits COHP peaks in the same energy range (Figure 4b). In contrast, the Au_{18e} 5d states occur in two energy ranges, from −6.9 to −5.8 eV and from −3.1 to −2.3 eV, and are responsible for the two major COHP contributions of Au_{18e}−Au_{18e} bonding within triangular units.

The COHP data (electronvolts per bond per mole) and the integrated Hamilton populations ICOHP provide some

dx.doi.org/10.1021/ja401378q | J. Am. Chem. Soc. 2013, 135, 11023−11031

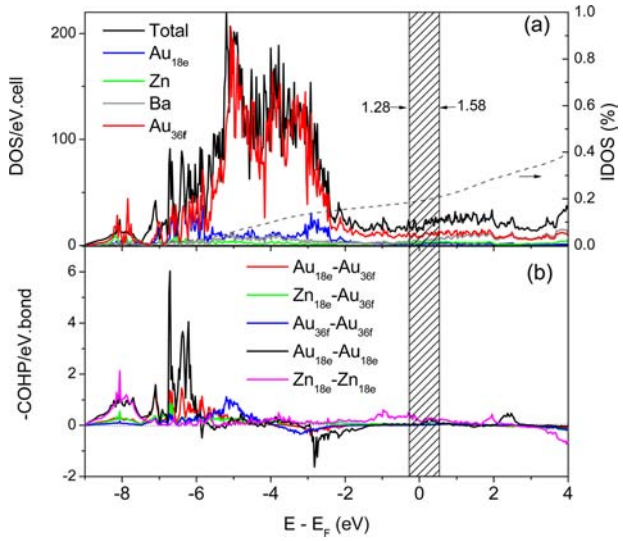

Figure 4. (a) Projected and total densities of states (DOS) for $Ba_2Au_7Zn_2$ in a model with ordered Au_3 and Zn_3 triangles and $P\bar{3}c1$ symmetry. The shaded region represents the Fermi energies for the range of refined compositions in the Zn system under rigid band assumptions. The dashed line represents the integration of Ba DOS on a scale of 0–1. (b) COHP data for five DOS components in the $Ba_2Au_7Zn_2$ model. Subscripts in both plots denote the Wyckoff site types. Bonding between three different Wyckoff set types in the Au lattice and the Au_3 and Zn_3 units is particularly evident.

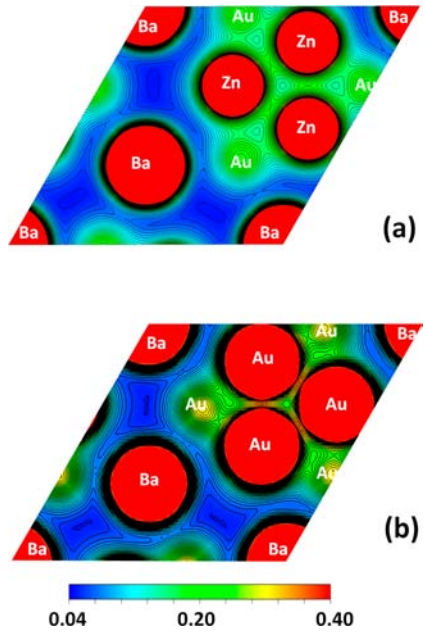

Figure 5. Evidence of electron delocalization in charge density sections through the planar Zn_3 and Au_3 units in the hypothetical ordered model for $Ba_2Au_7Zn_2$ ($P\bar{3}c1$). The contour lines are drawn between 0.04 and 0.40 $e^-/Å^3$ with spacings of 0.01 $e^-/Å^3$. Yellow areas in panel b labeled Au mark the passage of Au–Au pillar bonds in the gold host lattice through this section (see Figure 3b).

measure of importance for different bonds in this Zn model (Table 4). (Remember that these all come from a less stable model derived to achieve ordered Au_3 and Zn_3 units, so intercomparisons are somewhat "apples and oranges".) Values for Au–Au, Au–Zn, and Zn–Zn bonding are roughly inversely proportional to their respective bond distances; that is, the larger ICOHP values correspond to shorter bonds and presumably stronger interactions. The average interactions of the gold lattice with the mixed triangular units yield the two largest ICOHP values per contact [~1.6 eV/bond (Table 4)] followed by two more at 1.23 eV/bond for the shortest Au–Au bonds within the gold network (Figure 2), within the small hexagonal ring (~ 2.91 Å), and for Au–Au interlayer (pillar) bonding (0.8 eV/bond). The Au–Au bonding interactions in the large hexagonal rings in the gold lattice [3.142 Å (Figure 3)] correspond to an ICOHP value of 0.6 eV/bond, close to the upper limit among the polar Ba–Au bonding groups (0.45–0.17 eV/bond). This ordering of these populations relative to distance, function, and the elements involved is more or less typical among other such ternary gold (or platinum) compounds, but their relative magnitudes also depend appreciably on the particular structure and the gold, etc., proportions in each.[26,31]

A clearer view of the extent of the corresponding charge delocalization within the anionic network comes from the results of charge density calculations on the same ordered $Ba_2Au_7Zn_2$ model. Figure 5 shows two sections of the charge densities, through (a) the Zn_3 and (b) the Au_3 triangular interstitial models therein. [Recall also that these are separated along the *c* axis by two Ba cations (Figure 2).] The charge densities are both scaled over the range of 0.04–0.40 $e^-/Å^3$ (see color scale) with contour intervals of 0.01 $e^-/Å^3$. Therefore, the red spherical regions denote charge densities of >0.4 $e^-/Å^3$, with core states of the respective atoms at their centers, as marked. Note that three Au–Au pillars roughly along the *c* axis that surround each Zn_3 and Au_3 unit also go through these sections and are likewise marked by a white Au symbol. In these cases, the Au symbols do not mark Au core states, but the centers of the nominally linear pillar bonds (Figures 2 and 3b) that cross through this section, outside of the edges of the triangular interstitial units.

Interesting features of these charge density maps are the notable amounts of apparent electron delocalization within the triangular units (and between these and the hexagonal-diamond-like network in other sections). Perhaps the most intuitive evidence is the presence of broad green or green-to-yellow patches (higher charge density) that stand out from the blue "rivers" (lower density), lying outside the edges of the equilateral Au_3 and Zn_3 triangles in panels a and b of Figure 5. Some more general manifestations of electron delocalization can be judged from the more classical means, i.e., the contour lines. For Zn_3 as an example, the density at the center of the Zn_3 triangle in Figure 5a is a classical signature, whereas the three densities lying at approximately the centers of $AuZn_2$ atom groups express the electron delocalization between the pillars and Zn_3 units. Similar and more pronounced scenarios are observed around Au_3 units (Figure 5b). Of course, these are also consistent with the larger Hamilton bond populations between the M_3 and gold network atoms (Table 4).

Finally, it is worth noting that this structure is new in many ways, and close precedents for the bonding and delocalization therein are not immediately obvious. This is the first time we have looked directly at delocalization effects in any of the "polar intermetallics" we have discovered, which as a group are new and novel in a chemical sense because of the large differences in the chemistry and electronegativity of the components. This example is also a somewhat exceptional polar intermetallic because of its structure and high gold content. These phases are certainly well removed from typical metals and their more

dx.doi.org/10.1021/ja401378q | J. Am. Chem. Soc. 2013, 135, 11023–11031

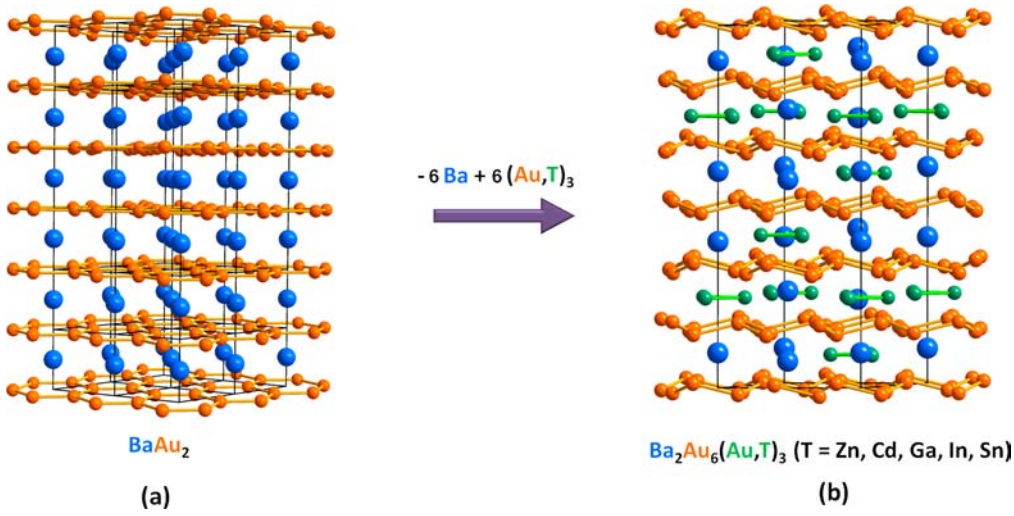

Figure 6. Topological relationship between (a) a 2 × 2 × 6 supercell of $BaAu_2$ and (b) the unit cell of $Ba_2Au_6(Au/T)_3$ (T = Zn, Cd, Ga, In, or Sn), which are related by an overall atom−triad exchange. The origin for $BaAu_2$ is shifted to (0 0 $^1/_2$) for the comparison.

familiar compounds and alloys, yet the high coordination numbers and electron delocalization are broad common features. Sometimes exploration leads the way.

Structure Relationship with $BaAu_2$. At first, one might assume that certain structural relationships should exist between the 2−6−3 structure and $BaAu_5$ (=Ba_2Au_{10})[32] because the latter has a similar elemental proportion. However, the Au_5^{2-} lattice in $BaAu_5$ is an extended network of corner-shared trigonal bipyramids, a different structural motif. In fact, the hexagonal-diamond-like Au lattice in the present 2−6−3 structure resembles more the In_2^{2-} anionic lattices in $CaIn_2$-type structures ($P6_3/mmc$),[30] regardless of the Au lattice puckering along the (001) direction allowed by the $R\bar{3}c$ symmetry. In addition, both $CaAu_2$ and $SrAu_2$ form $CeCu_2$-type structures,[27] in which the Au lattice also resembles that of the In_2^{2-} lattice in $CaIn_2$ except that "ladders" are formed in these. These facts encouraged us to check the structural relationship with $BaAu_2$.

The structure of $BaAu_2$ ($P6/mmm$, AlB_2-type) (Figure 6a)[33] features planar honeycomb Au nets in which each Au is bonded to three Au neighbors (2.753 Å). Neighboring Au nets are separated by ∼4.2 Å along the c axis, the unit cell height, by intervening Ba layers, meaning that essentially no bonding interactions occur between Au layers. In fact, a 2 × 2 × 6 supercell of $BaAu_2$ is comparable in size to the 2−6−3 unit cell and has topologically similar layered motifs (Figure 6) if the bonds in 2−6−3 structures are limited to those of <3.0 Å. Actually, the reordered formula $(Ba_2M_3)Au_6$ clearly describes the topological substitution relationship with Ba_3Au_6 (=$3BaAu_2$), in which one of three Ba atoms is replaced with an M_3 [or $(Au,T)_3$] triangle. Although substitution of electropositive Ba atoms with electronegative M_3 units is chemically implausible, intriguing atom-by-triad substitutional phenomena have been reported to occur to limited degrees in AlB_2-type $Sr_{1-x}Ga_{2+3x}$[34] and $U_3Ni_4Si_4$-type $M_{3-x}Ga_{8+3x}$ (M = Yb,[35] Eu,[36] or Sr[37]). What is unique about the 2−6−3 phases presented here is that one-third of Ba atoms in $BaAu_2$ are changed into an equal number of associated $(Au,T)_3$ groups in the resulting superstructure, whereas atom-by-triad substitutions in the foregoing Ga phases take place at a frequency of <15%, giving substitutionally defective structures.

CONCLUSIONS

In summary, we have discovered series of very unusual 2−6−3 phases [$Ba_2Au_6(Au,T)_3$ for T = Zn, Cd, Ga, In, or Sn] that exhibit both novel structural and electronic structure features via ordered Ba and triangular $(Au,T)_3$ interstitials in a rhombohedral superstructure of a simple but unknown h.c.p. Au lattice. All of these phases show limited ranges of composition and electron count variations within disordered $(Au,T)_3$ components, as exemplified in the extreme in the Zn system in which the mixtures range from ∼31 to 87% Zn. Single-crystal analyses reveal that these structures contain unprecedented hexagonal-diamond-like gold lattices in which tunnels along the c axis are filled by ordered Ba atoms and triangular $(Au,T)_3$ interstitials. These hexagonal-diamond-like gold lattices can be topologically derived from $BaAu_2$ (AlB_2-type) by means of a homogeneous atom-by-triad substitution, i.e., Ba with $(Au,T)_3$. Theoretical analyses of ordered versions of the broader Zn system suggest a significantly delocalized and moderately polarized electronic system in these 2−6−3 examples.

ASSOCIATED CONTENT

Supporting Information

Crystal and refinement parameters for $Ba_2Au_6(Au,T)_3$ (T = Cd, Ga, In, and two Zn phases) (Tables S1 and S2); selected bond distances for T = Cd, Ga, In, and Sn (Table S3); atomic positions for the $Ba_2Au_7Zn_2$ model used in LMTO calculations (Table S4); observed and calculated X-ray powder diffraction patterns for T = Cd, Ga, In, and Sn samples [Figure S1 (four parts)]; plot of observed lattice constants for refined $Ba_2Au_6(Au_{3-y}Zn_y)$ phases (Figure S2); an illustration of the network "wobbling" in the 3-fold tunnels along the c axis (Figure S3); (001) projection of a single puckered Au layer in Ba_2Au_8Sn with dimensions (Figure S4); and cif outputs. This material is available free of charge via the Internet at http://pubs.acs.org.

AUTHOR INFORMATION

Corresponding Author

jcorbett@iastate.edu

Notes

The authors declare no competing financial interest.

■ ACKNOWLEDGMENTS

This research was supported by the U.S. National Science Foundation, Solid State Chemistry, via Grant DMR-0853732. All of the work was performed in the facilities of the Ames Laboratory, U.S. Department of Energy.

■ REFERENCES

(1) Wade, K. *Adv. Inorg. Chem. Radiochem.* **1976**, *18*, 1.
(2) Kauzlarich, S. M., Ed. *Chemistry, Structure, and Bonding of Zintl Phases and Ions*; VCH: New York, 1996.
(3) Hume-Rothery, W.; Raynor, G. V. *The Structure of Metals and Alloys*, 4th ed.; Institute of Metals: London, 1962.
(4) Mizutani, U. *Hume-Rothery Rules for Structurally Complex Alloy Phases*; CRC Press: London, 2011.
(5) Lin, Q.; Corbett, J. D. *J. Am. Chem. Soc.* **2007**, *129*, 6789.
(6) Lin, Q.; Corbett, J. D. *Inorg. Chem.* **2008**, *47*, 7651.
(7) Lin, Q.; Corbett, J. D. *Inorg. Chem.* **2010**, *49*, 10436.
(8) Lin, Q.; Corbett, J. D. *Inorg. Chem.* **2010**, *49*, 4570.
(9) Lin, Q.; Smetana, V.; Miller, G. J.; Corbett, J. D. *Inorg. Chem.* **2012**, *51*, 8882.
(10) Smetana, V.; Lin, Q.; Pratt, D. K.; Kreyssig, A.; Ramazanoglu, M.; Corbett, J. D.; Goldman, A. I.; Miller, G. J. *Angew. Chem., Int. Ed.* **2012**, *51*, 12699.
(11) Corbett, J. D. *Inorg. Chem.* **2010**, *49*, 13.
(12) Li, B.; Kim, S.-J.; Miller, G. J.; Corbett, J. D. *Inorg. Chem.* **2009**, *48*, 6573.
(13) Lin, Q.; Corbett, J. D. *J. Am. Chem. Soc.* **2010**, *132*, 5662.
(14) Lin, Q.; Corbett, J. D. *Inorg. Chem.* **2007**, *46*, 8722.
(15) Lin, Q.; Corbett, J. D. *Inorg. Chem.* **2011**, *50*, 1808.
(16) Lin, Q.; Corbett, J. D. *J. Am. Chem. Soc.* **2012**, *134*, 4877.
(17) Pyykkö, P. *Angew. Chem., Int. Ed.* **2004**, *43*, 4412.
(18) Lin, Q.; Corbett, J. D. *Inorg. Chem.* **2008**, *47*, 3462.
(19) Kraus, W.; Nolze, G. In *Powder Cell for Windows* (http://www.bam.de/de/service/publikationen/powder_cell.htm).
(20) Holland, T. J. B.; Redfer, S. A. T. *Mineral. Mag.* **1997**, *61*, 65.
(21) *SHELXTL*, version 6.10; Bruker Analytical X-ray Systems, Inc.: Madison, WI, 2000.
(22) Andersen, O. K.; Jepsen, O. *Phys. Rev. Lett.* **1984**, *53*, 2571.
(23) Shriver, H. L. *The LMTO Method*; Springer-Verlag: Berlin, 1984.
(24) Tank, R.; Jepsen, O.; Burkhardt, A.; Andersen, O. K. *TB-LMTO-ASA*, version 4.7; Max-Planck-Institut für Festkörperforschung: Stuttgart, Germany, 1994.
(25) Dronskowski, R.; Bloechl, P. E. *J. Phys. Chem.* **1993**, *97*, 8617.
(26) Samal, S. L.; Pandey, A.; Johnston, D. C.; Corbett, J. D. *J. Am. Chem. Soc.* **2013**, *135*, 910.
(27) Villars, P.; Calvert, L. D. *Pearson's Handbook of Crystallographic Data for Intermetallic Phases*, 2nd ed.; American Society of Metals: Materials Park, OH, 1991; Vol. *1*.
(28) Lonsdale, K. *Am. Mineral.* **1971**, *56*, 333.
(29) Frondel, C.; Marvin, U. B. *Nature* **1967**, *214*, 587.
(30) Zhang, H.; Borrmann, H.; Oeschler, N.; Candolfi, C.; Schnelle, W.; Schmidt, M.; Burkhardt, U.; Baitinger, M.; Zhao, J.-T.; Grin, Y. *Inorg. Chem.* **2011**, *50*, 1250.
(31) Samal, S. L.; Gulo, F.; Corbett, J. D. *Inorg. Chem.* **2013**, *52*, 2697.
(32) Palenzona, A.; Bonino, G. B. *Atti Accad. Naz. Lincei, Cl. Sci. Fis., Mat. Nat., Rend.* **1967**, *42*, 504.
(33) Bruzzone, G. *Atti Accad. Naz. Lincei, Cl. Sci. Fis., Mat. Nat., Rend.* **1970**, *48*, 235.
(34) Haarmann, F.; Prots, Y. *Z. Anorg. Allg. Chem.* **2006**, *632*, 2135.
(35) Cirafici, S.; Fornasini, M. L. *J. Less-Common Met.* **1990**, *163*, 331.
(36) Sichevich, O. M.; Prots, Y.; Grin, Y. *Z. Kristallogr.* **2006**, *221*, 265.
(37) Haarmann, F.; Prots, Y.; Gobel, S.; von Schnering, H. G. *Z. Kristallogr.* **2006**, *221*, 257.